Available online at www.sciencedirect.com
SCIENCE DIRECT®
Journal of Chromatography A, 1030 (2004) 53–62
JOURNAL OF CHROMATOGRAPHY A
www.elsevier.com/locate/chroma

Computational study of the band broadening in two-dimensional etched packed bed columns for on-chip high-performance liquid chromatography

P. Gzil*, J. De Smet, N. Vervoort, H. Verelst, G.V. Baron, G. Desmet

Department of Chemical Engineering, Vrije Universiteit Brussel, Pleinlaan 2, 1050 Brussels, Belgium

Abstract

The chromatographic performance of several straightforward two-dimensional etched packed bed column lay-outs (equilaterally staggered arrays of, respectively, circular, hexagonal, and diamond-like pillars) has been compared using commercial computational fluid dynamics software. In all cases, the bed porosity was kept at $\varepsilon = 0.4$ and a retained component with zone capacity ratio $k'' = 2$ was considered. Exploring the use of six different possible characteristic dimensions to bring the Van Deemter plots of the three different considered particle shapes into agreement, none of them yielded a perfect agreement. Using the pillar volume-based equivalent cylinder diameter (d_{eq}) as the characteristic dimension, the diamond-like pillars yielded a significantly smaller h_{min} value than the cylinders and the hexagons ($h_{min} \cong 0.74$ for the former versus $h_{min} \cong 0.83$ for the two latter). Including the flow resistance into the analysis, it was found that the "hydrodynamic" shape of the particles has an important influence on the separation impedance E. The more axially elongated diamond pillars yielded an E_{min} number as small $E_{min} = 180$ (for a retained component with $k'' = 2$), i.e. about 40% smaller than the cylinders and the hexagons ($E_{min} = 300$–330). The obtained h_{min} and E_{min} values are also significantly smaller than the values often cited for the best possible packed bed HPLC columns. We believe this is a consequence of the assumed perfect homogeneity of the etched structures, and hence hints at the potential benefits of perfectly ordered chromatographic columns, as was already inferred by Knox [J. Chromatogr. A 831 (1999) 3; 960 (2002) 7] and He et al. [Anal. Chem. 70 (1998) 3790].

Keywords: Band broadening; Computational fluid dynamics; Packed columns; Etched columns; Mathematical modelling; Computer simulation

1. Introduction

In two relatively recent papers, Knox [1,2] mentioned the use of two-dimensional (2D) etched columns as an attractive possibility to obtain significantly smaller reduced plate heights than what is possible with the best possible packed bed columns. He thereby especially foresaw a large possible reduction of the A term, due to the high degree of regularity with which the packings can be machined. His suggestion in fact follows upon the ground-breaking work of He et al. [3] who first pointed out the possibility of micro-machined packed columns to the chromatographic community. Apart from the increased packing homogeneity and the superfluity of frits, the micro-machined column concept also opened the road to a quasi-unlimitedly large variety of possible particle shapes and particle arrangements, a possibility which was up to then quasi unexplored in the field of LC. Using an argument based on an optimisation of the number of trans-channel coupling points, a densely packed array of cubic structures was suggested as the ideal column format [3,4]. This was subsequently confirmed under electrically-driven flow conditions, but the results were found to depend strongly on imperfections of the etched packing structures [5]. Tests under pressure-driven conditions have not been carried out yet, but it can be expected that in that case, the trans-channel coupling points will play an even more important role.

Given the large degree of design freedom (structure shape, packing density, relative positioning of the etched structures, etc.), the lack of a well-established band broadening expression, and the large experimental cost of a broad-scale explorative study, the present paper reports on the use of a commercial computational fluid dynamics (CFD) software package to study the band broadening in 2D periodic chromatographic packings. With the exponential increase in computational power, it has now namely become possible to solve the complete impulse and species conservation balances determining the flow and band broadening processes

* Corresponding author. Tel.: +32-2-629-32-51; fax: +32-2-629-32-48.
E-mail address: pgzil@vub.ac.be (P. Gzil).

0021-9673/$ – see front matter © 2004 Elsevier B.V. All rights reserved.
doi:10.1016/j.chroma.2003.12.038

in chromatographic columns in its full detail and without having to make any simplifying assumption. Combining advanced grid generation algorithms (used to divide the flow domain in a large number of small calculation cells wherein the complete impulse and species balances are solved numerically) with a powerful numerical solver and a wide range of data post-processing possibilities (graphical representation, calculation of averaged values, etc.), CFD packages are especially suited to calculate the velocity field in complex geometries and provide unique data on the flow and species transport on scales which are inaccessible to experimental measurement methods. CFD simulations have therefore also become an increasingly used design tool in the lab-on-a-chip field [6,7] and for the analysis of the flow pattern in chromatographic columns [8–11]. Since the flow in an LC column is without any doubt purely laminar, and is hence purely deterministic, the CFD results can be made fully accurate, provided care is taken that the obtained results are independent of the grid shape and size.

The specific aim of the present study was three-fold: (i) obtain information on the theoretical plate heights and Knox parameters which can be achieved in 2D etched columns; (ii) gain insight in the selection of the appropriate characteristic dimensions bringing the flow resistance and band broadening of differently shaped chromatographic particles into agreement; and (iii) investigate the influence of the particle shape on the minimal plate height and the separation impedance (cf. the E number). Although such columns do not exist yet (the COMOSS structures used in Regnier's group have non-porous pillars), the present study focuses on porous pillar systems because we wanted to compare the obtained plate heights and separation impedances directly to real (three-dimensional, 3D) packed bed columns containing porous particles.

2. Considered geometries and performance comparison criteria

At present, we have limited our study to three different pillar shapes (cf. Fig. 1): cylinders, equilateral hexagons and diamonds with a $d_{ax}/d_{lat} = \sqrt{3}$ diagonal ratio. To focus entirely on the influence of the particle shape, other geometrical parameters such as the bed porosity and the pillar arrangement were kept constant: in all considered cases, the bed porosity was exactly equal to $\varepsilon = 0.4$, and the pillars were always arranged in an equilateral staggered configuration, i.e. the centre points of neighbouring pillars are situated on the corners of an equilateral triangle. With these restrictions, the unit cell domain retains the same width over length ratio (d_{dom}/L_{dom}) for all three considered particle shapes. The ratio also remains unchanged when the dimensions of a given particle are changed (cf. the different cases shown in Fig. 1). The imposed geometrical restrictions also limit the number of diamond shapes which can be selected. Square-shaped pillars, for example, do not fit into an equilaterally staggered configuration. Table 1 gives an overview of the geometrical relations between the characteristic dimensions of the pillar arrays on the one hand and the main characteristic dimension (diameter d_p for cylinders and side length s for the hexagons and diamonds) of the three different pillar shapes on the other hand.

One of the initial questions immediately arising when intending to explore the possibilities of alternative particle shapes is what characteristic dimension d_{ref} needs to be considered to make a correct comparison between the different systems, i.e. to bring the reduced Van Deemter plots for the different considered geometries into agreement. For a packed bed of particles or for a cylindrical pillar system, the selection of d_{ref} is obvious, but for non-circular or

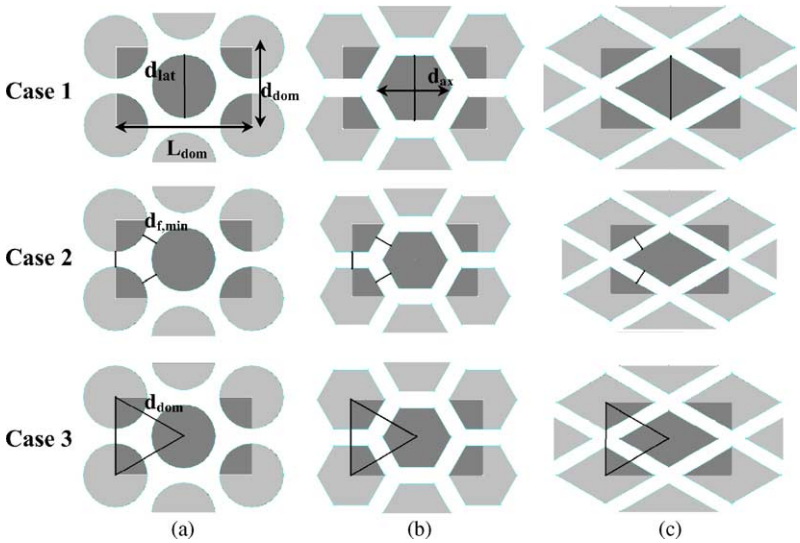

Fig. 1. Overview of the unit cells of the considered pillar arrangements for the three different considered pillar shapes: (a) cylinders; (b) equilateral hexagons; (c) diamond-like pillars. For each pillar shape, three of the six cases considered in Table 2 are represented.

Table 1
Geometrical parameter values for the different considered pillar shapes in relation to their main characteristic dimension (diameter d_p for cylinders and side length s for the hexagons and diamonds) and the bed porosity

	Cylinders	Hexagons	Diamonds
d_{lat}	d_p	$\sqrt{3}s$	s
d_{ax}	d_p	$2s$	$\sqrt{3}s$
d_{eq}	d_p	$\sqrt{\frac{6\sqrt{3}}{\pi}s}$	$\sqrt{\frac{2\sqrt{3}}{\pi}s}$
$d_{f,min}$	$d_{dom} - d_p$	$d_{dom} - \sqrt{3}s$	$\frac{1}{2}\sqrt{3}(d_{dom} - s)$
$d_{f,mean}$	$\frac{1}{2}\frac{\varepsilon d_{dom}}{\tau}$	$\frac{1}{2}\frac{\varepsilon d_{dom}}{\tau}$	$\frac{1}{2}\frac{\varepsilon d_{dom}}{\tau}$
$d_{FR,eq}$	d_{eq}	$1.039d_{eq}$	$1.210d_{eq}$
d_{dom}	$\sqrt{\frac{\pi}{2\sqrt{3}}\frac{1}{1-\varepsilon}}d_p$	$\frac{\sqrt{3}}{\sqrt{1-\varepsilon}}s$	$\frac{s}{\sqrt{1-\varepsilon}}$
L_{dom}	$\sqrt{3}d_{dom}$	$\sqrt{3}d_{dom}$	$\sqrt{3}d_{dom}$
P	πd_p	$6s$	$4s$
A_p	$\frac{1}{4}\pi d_p^2$	$\frac{3}{2}\sqrt{3}s^2$	$\frac{3}{2}\sqrt{3}s^2$
S_p/V_p	$\frac{4}{d_p}$	$\frac{4}{\sqrt{3}s}$	$\frac{8}{\sqrt{3}s}$
S_p/V_f	$\frac{4}{d_p}\frac{1-\varepsilon}{\varepsilon}$	$\frac{4}{\sqrt{3}s}\frac{1-\varepsilon}{\varepsilon}$	$\frac{8}{\sqrt{3}s}\frac{1-\varepsilon}{\varepsilon}$
t[a]	1.221	1.248	1.122

[a] Values numerically calculated in the present study (see text).

non-spherical particles this is no longer the case. This is a problem which is, for example, also encountered [12–14] when trying to bring the band broadening in monolith columns into agreement with that in packed beds.

To help find the appropriate characteristic dimension for the presently considered 2D packings, six different straightforward cases have been considered: case 1, wherein the pillars have the same maximal lateral width (d_{lat}); case 2, wherein the minimal distance ($d_{f,min}$) between the pillars is identical; case 3, wherein the domain size (d_{dom}) is identical; case 4, wherein the pillar dimensions are selected such that identical bed permeabilities are obtained; case 5, wherein the pillars have the same specific outer surface ($a = S_p/V_p$); and case 6, wherein the mean flow-through pore size is kept constant ($d_{f,mean}$). The relative relations between the different considered cases are given in Table 2. Cases 1–3 are also schematically represented in Fig. 1.

As can be noted from Fig. 1, the domain size (d_{dom}) is defined as the distance between the centre points of two neighbouring pillars. It should be noted here that, within the presently considered geometry (i.e. $\varepsilon = 0.4$ and an equilateral staggered pillar arrangement for all three considered pillar shapes), the condition of a constant domain size (case 3) is only possible if the cross-sectional area (A_p) of the individual pillars is also equal. Case 3 hence also corresponds to the case of identical cross-sectional pillar area. For the hexagons and diamonds, it is under the condition of case 3 hence straightforward to define an equivalent cylinder diameter (d_{eq}) as the diameter of the cylinder having the same cross-sectional area as the hexagon or diamond with given A_p:

$$d_{eq} = \sqrt{\frac{4}{\pi}A_p} \quad (1)$$

All this information is also contained in Table 2: the rows for case 3 (constant d_{dom}) also have identical entries in the columns for d_{eq} and for the cross-sectional pillar area A_p.

In case 6, the different pillar systems are compared on the basis of an identical mean flow-through pore size $d_{f,mean}$. Finding a mathematical expression for the latter is, however, not straightforward to find. In the present study, we defined $d_{f,mean}$ as the ratio of the cross-sectional pore area A_f (cross-section taken in the xy-plane) to the pore length. The cross-sectional pore area A_f can simply be calculated from the total domain size using $A_f = 0.5A_{dom}\varepsilon$. The factor 0.5 stems from the fact that the fluid zone in the unit cells depicted in Fig. 1 in fact contain two pores, just like it

Table 2
Relations between a number of important characteristic dimensions for the six different considered cases

	d_{lat}	$d_{f,min}$	d_{dom}	$d_{FR,eq}$	S_p/V_p	$d_{f,mean}$	P	A_p	d_{eq}	d_{ax}	S_p/V_f
Cylinders	1.000	0.229	1.229	1.000	4.000	0.201	3.142	0.785	1.000	1.000	6.000
Hexagons											
Case 1	1.000	0.291	1.291	1.091	4.412	0.207	3.466	0.825	1.050	1.155	6.619
Case 2	0.787	0.229	1.016	0.859	3.472	0.163	2.728	0.649	0.827	0.909	5.209
Case 3	0.952	0.277	1.229	1.039	4.200	0.197	3.300	0.785	1.000	1.100	6.301
Case 4	0.916	0.267	1.183	1.000	4.042	0.190	3.176	0.756	0.962	1.059	6.064
Case 5	0.907	0.264	1.171	0.990	4.000	0.188	3.143	0.748	0.952	1.048	6.001
Case 6	0.973	0.283	1.256	1.060	4.285	0.201	3.367	0.801	1.020	1.122	6.429
Diamonds											
Case 1	1.000	0.252	1.292	1.271	5.095	0.230	4.001	0.825	1.050	1.732	7.642
Case 2	0.908	0.229	1.174	1.155	4.628	0.209	3.634	0.749	0.954	1.573	6.942
Case 3	0.952	0.240	1.229	1.210	4.850	0.219	3.809	0.785	1.000	1.649	7.275
Case 4	0.787	0.198	1.017	1.000	4.008	0.181	3.148	0.649	0.826	1.363	6.012
Case 5	0.785	0.198	1.014	0.998	4.000	0.181	3.141	0.647	0.825	1.360	6.000
Case 6	0.874	0.220	1.129	1.111	4.451	0.201	3.496	0.720	0.918	1.513	6.677

The underlined values refer to the dimension kept constant in the given case.

contains two pillars. The pore length is then subsequently estimated from the product of the domain length L_{dom} and the pore tortuosity τ. With these geometrical data, it is now obvious to calculate the mean pore diameter as the ratio of the cross-sectional area and its tortuous path length, yielding:

$$d_{f,mean} = \frac{1}{2}\frac{A_{dom}\varepsilon}{L_{dom}\tau} \quad (2)$$

The calculation of τ (values given in the bottom row of Table 1) requires the solution of the velocity field and is discussed in Section 4.1. The definition and calculation of d_{FR} (case 4) is given in Section 4.1 as well.

All different considered cases are compared on the basis of two widely used criteria: the minimal reduced plate height (h_{min}), and the separation impedance (E), defined as:

$$E = \frac{H^2}{K_v} = h^2\phi \quad (3)$$

wherein K_v is the column permeability:

$$K_v = \frac{u_0\eta L}{\Delta P} \quad (4)$$

which is often also expressed in terms of the flow resistance factor ϕ defined as:

$$\phi = \frac{d_{ref}^2}{K_v} \quad (5)$$

3. Numerical solution and data processing methods

Flow domains corresponding to the geometries described in Fig. 1 and Tables 1 and 2 were designed using a commercial CAD program (GAMBIT v.2), acting at the same time as the grid generator for the FLUENT 6.0 CFD software package used to solve the exact flow and species diffusion equations governing the complete chromatographic process [15]. The exact dimensions of the considered flow domains can be retrieved by multiplying the data given in Table 2 by a factor 3×10^{-6} m, i.e. the simulations carried out for case 3, for example, all corresponded to pillars with an equivalent cylinder diameter of $d_{eq} = 3\,\mu m$.

For each case, first a representative unit cell (cf. the dark grey areas in Fig. 1) was designed, which was then subsequently replicated and translated to form a flow domain consisting of a series connection of 10 unit cells. So-called velocity-inlet and pressure-outlet conditions were, respectively, imposed at the front and end plane of the flow domain. Along the side-walls, a zero normal concentration gradient condition was imposed. With this condition of symmetry, the considered flow domain behaves as if it were embedded in an infinitely wide structure. For the same reason, the parts of the side-walls occupied by the fluid zone were subjected to a slip flow boundary condition (zero normal velocity gradient) to calculate the velocity field. At the surfaces of the porous particles, a no-slip boundary condition ($u = 0$ at the wall surface) was imposed to account for the flow arresting effect of the solid pillar surfaces. Further setting up the problem for the CFD software, the pillar zones were defined as porous zones. Within the software program, porous zones are attributed a freely selectable flow resistance factor, but this was always set at infinity in the present study to mimic the absence of any intra-particle convection. Each individual pillar zone was subsequently also defined as being embedded in a continuous fluid zone, corresponding to the total surface area of the flow domain which is not occupied by the pillars. The effect of the internal porosity of the pillar zones can easily be reproduced, as the software package has a built-in function allowing to attribute a given, freely selectable, internal porosity to the porous zones. To approximate the conditions in a traditional packed bed column, a value of $\varepsilon_{int} = 0.5$ has been assumed in all presented calculations.

The software package was further extended with a number of self-written numerical routines to simulate the diffusion and adsorption processes inside the porous pillars. A first user defined function was written to mimic the effect of the slow intra-particle diffusivity. The function was used to attribute the species entering the stationary phase zones a diffusion coefficient different (i.e. smaller) from that in the fluid zone. In all presented cases, the stationary phase diffusion coefficient D_s was always put at $5 \times 10^{-10}\,m^2/s$, whereas the mobile zone diffusion coefficient was always set at $D_m = 1 \times 10^{-9}\,m^2/s$. The liquid phase viscosity was always put at $\eta = 10^{-3}\,kg/(m\,s)$.

A second user defined function was written to represent the selective adsorption (retention) of the species in the stationary phase zones. This process was mimicked by subjecting the species present in the porous pillar zones to a reversible chemical reaction transforming the freely diffusing species Y into a species Y* with identical physical properties but with a zero diffusivity, as to express its adsorbed state:

$$Y\ (\text{freely diffusing}) \underset{k_2}{\overset{k_1}{\rightleftarrows}} Y^*\ (\text{adsorbed}) \quad (6)$$

By changing the ratio K of the forward and backward rate constant, different adsorption equilibria can be imposed, which in turn corresponds to a variation of the phase and zone retention factors (k' and k''). In all the presented calculations, K was always selected such that a zone retention factor $k'' = 2$ was obtained. From the known external (ε) and internal (ε_{int}) porosities, the zone retention factor k_0'' of the unretained species (i.e. species for which $K = 0$) can easily be calculated to be given by:

$$k_0'' = \left(\frac{1-\varepsilon}{\varepsilon}\right)\varepsilon_{int} = 0.75 \quad (7)$$

All calculations were carried out on Dell personal computers with Intel Xeon 2 GHz processor, and equipped with 2 GB RAM. To ensure that the velocity fields calculated by the CFD software were grid-independent, i.e. were independent

of the degree of discretisation of the flow domain, a velocity gradient adaptation of the grid was performed after the initial 100–300 iteration steps and before running another 200 iterations. The change in the velocity field values and pressure drop was smaller than 0.2%, small enough to conclude that the solutions are grid-independent and sufficiently converged. To ensure that the calculated species transport rates are grid- and time step-independent, a range of different grid sizes has been explored. It was found that, for the entire simulation domain (i.e. 10 unit cells in series), the use of about 25 000 cells was sufficient to achieve an accuracy of approximately 0.2% on the resulting plate height value.

The latter was obtained by monitoring the radially averaged species concentration response to the virtual injection of a plug of tracer species at nine successive detection planes, each positioned at the interface between two successive unit cells. From these concentration response curves, the peak migration time and the peak variance were assessed by numerically calculating the zeroth-, first- and second-order moment of the obtained break-through curves, using:

$$t_{\mathrm{R},i} = \frac{\int_0^{+\infty} C_i t \,\mathrm{d}t}{\int_0^{+\infty} C_i \,\mathrm{d}t} \tag{8}$$

$$\sigma_{t,i}^2 = \frac{\int_0^{+\infty} C_i t^2 \,\mathrm{d}t}{\int_0^{+\infty} C_i \,\mathrm{d}t} - t_{\mathrm{R}}^2 \tag{9}$$

From Eq. (8), the phase and zone retention factors (k' and k'') can be calculated as:

$$t_{\mathrm{R},i} = \frac{L_i}{u_0}(1 + k') = \frac{L_i}{u_{\mathrm{m}}}(1 + k'') \tag{10}$$

wherein u_{m} is the mean axial component of interstitial fluid velocity, and u_0 the migration velocity of the non-retained species. Both characteristic velocities are related by the zone retention factor k_0'' of the unretained species:

$$u_0 = \frac{u_{\mathrm{m}}}{1 + k_0''} \tag{11}$$

From Eqs. (8) and (9), the theoretical plate height values could be directly calculated using:

$$H = \frac{\sigma_{t,j}^2 - \sigma_{t,i}^2}{(t_{\mathrm{R},j} - t_{\mathrm{R},i})^2} L_{ij} \tag{12}$$

To validate the adopted modelling and flow simulation techniques, we first calculated the chromatographic band broadening for a case for which an analytical solution is available. Considering an open-tubular channel with flat-rectangular cross-section with a thickness $d = 2\,\mu\mathrm{m}$ and coated with a stationary phase with thickness $d = 1\,\mu\mathrm{m}$ and a zone retention factor of $k'' = 2$, and refining the employed computational grid size and time step such that they no longer influenced the end result, a perfect agreement with the theoretical Golay equation was obtained. With this validation, the simulation of the 2D etched packing structures could be attacked with confidence.

4. Results and discussion

4.1. Velocity fields and flow resistance

Fig. 2 shows the calculated velocity fields for the three different considered pillar shapes under the conditions of case 3. During the entire study, all simulated velocity fields were always characterised by calculating the volume-averaged velocity magnitude $\langle u \rangle$, the volume-averaged x-component of the velocity $\langle u_x \rangle$, the total volumetric flow rate Q passing through each cross-sectional plane of the unit cell and the

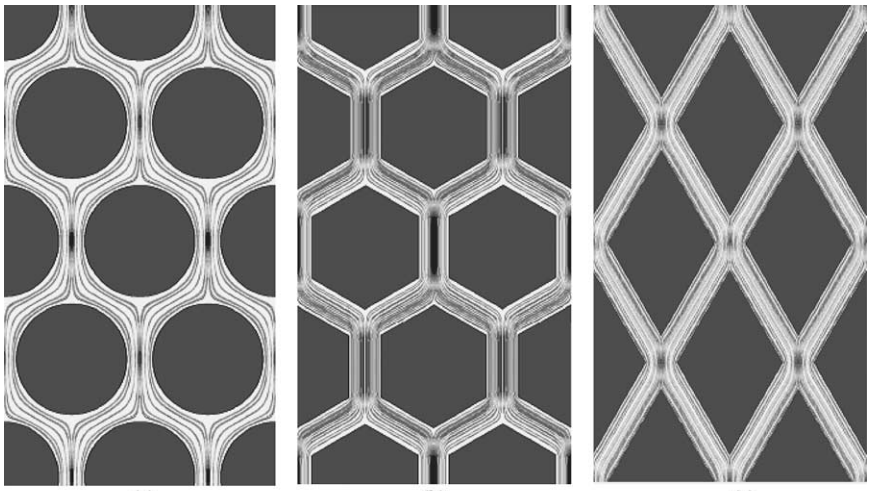

Fig. 2. Comparison of the calculated velocity fields for the three different considered pillar shapes under the condition of an identical domain size and cross-sectional particle area (case 3). The streamlines are coloured in relation to the local velocities.

total pressure gradient $\Delta P/L$. It should be noted here that the $\langle u_x \rangle$ velocity values correspond to the linear interstitial flow velocity traditionally used in pressure drop correlations and that the ratio of the flow rate Q (with dimensions m^2/s, since we are considering a 2D case) and the total width (d_{dom}) of the unit cell corresponds to the superficial velocity u_{sf}:

$$u_{sf} = \frac{Q}{d_{dom}} \tag{13}$$

The volume-averaged velocity magnitude $\langle u \rangle$ is a measure for the true interstitial velocity.

When considering the results of a CFD study, as many validity checks as possible have to be made to ensure that the appropriate numerical solution parameters (number and shape of cells, employed residual-drop criterion, values of the relaxation factors employed in the numerical scheme, etc.) have been selected. In the present study, several of such checks have been incorporated. From the theory of hydrodynamics, it is, for example, a well-known fact [16] that the $\langle u \rangle$ value is related to the $\langle u_x \rangle$ value via the bed tortuosity τ:

$$\tau = \frac{\langle u \rangle}{\langle u_x \rangle} \tag{14}$$

while the superficial velocity u_{sf} and the volume-averaged x-component of the velocity $\langle u_x \rangle$ are in turn related by the bed porosity:

$$\varepsilon = \frac{u_{sf}}{\langle u_x \rangle} \tag{15}$$

To verify the accuracy of our calculations, it was therefore always investigated whether the bed porosity calculated via Eq. (15) agreed with the bed porosity calculated on the basis of the dimensions of the considered flow domain. When the grid is too coarse, there might be a considerable discrepancy. In the cases presented here, the agreement was, however, always better than 1%. Another validity check was based on the bed tortuosity τ, for this quantity should namely depend exclusively on the geometry of the flow-through pore system and should hence be independent of the imposed velocity. Upon verification, it was indeed found that the τ values calculated on the basis of Eq. (14) were identical to within 0.5% when considering simulations performed for different velocities but in the same unit cell. Since the relative dimensions of the flow domains remain identical when passing from cases 1 to 6 for, it was also not surprising to find that all cases related to the same particle shape led to the same tortuosity. The obtained τ values are listed in Table 1 (bottom row).

At this point, it is also interesting to note that the cylindrical and the hexagonal pillars yield approximately the same value for τ ($\tau = 1.221$ for the cylinders versus $\tau = 1.248$ for the hexagons). This can readily be understood from the fact that the flow around the cylindrical pillars apparently spontaneously organises itself in a hexagon-like flow pattern, as can be noted from the calculated flow field in Fig. 2a.

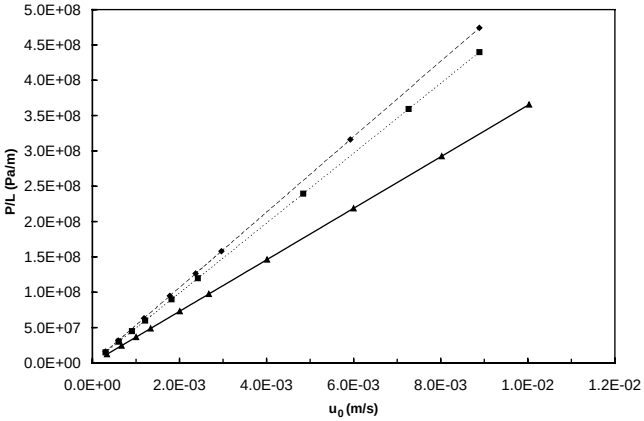

Fig. 3. Plot of ΔP vs. u_0 for the three different considered pillar shapes (case 3). Using the straight line slopes to calculate K_v from Eq. (4), the following values are obtained: $K_v = 2.08 \times 10^{-15}\,m^2$ (■, cylinders); $K_v = 2.25 \times 10^{-15}\,m^2$ (◆, hexagons); $K_v = 3.05 \times 10^{-15}\,m^2$ (▲, diamonds).

The slightly smaller τ value for the cylindrical pillars can be understood from the fact that the corners of the hexagonal flow pattern are slightly more rounded than in the hexagonal pillar case. The τ value for the diamonds is significantly smaller than for the two other pillar shapes ($\tau = 1.12$ versus $\tau = 1.22$–1.24). This can be understood from the fact that the diamonds are clearly more axially elongated than the two other bodies. This is also reflected in the calculated flow field shown in Fig. 2c.

Yet another validity check was based on the expected linear relation (cf. Darcy's law for the laminar flow through porous media) between the calculated pressure drop per length value ($\Delta P/L$) and the velocity u_0 of the unretained peak for simulations carried out on the same unit cell. As can be ascertained from Fig. 3, this is indeed the case. Fig. 3 (established for case 3) also clearly shows that a comparison on the basis of an identical domain size and particle cross-sectional area yields a different slope for the $\Delta P/L$ versus u_0 lines for each of the considered pillar shapes. As a consequence, the corresponding K_v values calculated on the basis of Eq. (4) yield a different value for the three different pillar shapes (data given in the caption of Fig. 3). This also implies that when calculating the flow resistance on the basis of the equivalent cylinder diameter d_{eq}:

$$\phi_{case\,3} = \frac{d_{eq}^2}{K_v} \tag{16}$$

three different values for ϕ are obtained (see Table 3). As can be noted, the difference between the flow resistance of

Table 3
Summary of the most relevant chromatographic performance parameters

	d_{ax}/d_{lat}	ϕ	Pe_{min}	h_{min}	A	B	C	E_{min}
Cylinders	1	480	5.5	0.833	0.064	2.060	0.061	333
Hexagons	1.154	445	5.5	0.830	0.058	2.025	0.065	306
Diamonds	1.732	328	6	0.737	0.027	2.089	0.056	178

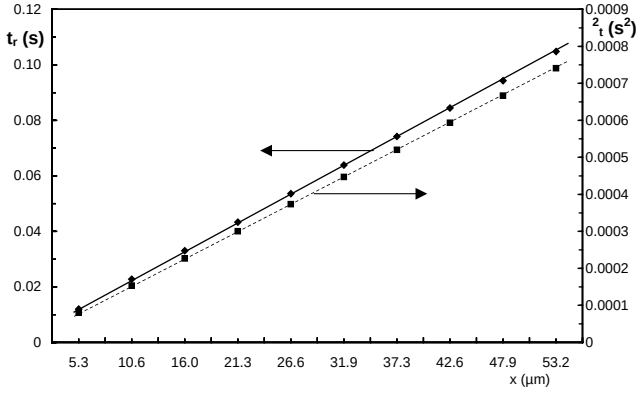

Fig. 4. Evolution of σ_x^2 (full lines) and t_r (dashed lines) with x for one of the considered cylindrical pillar domains (case 1, $u_0 = 0.93$ mm/s).

the cylinders and hexagons is relatively small, whereas the diamonds yield a significantly smaller flow resistance ($\phi =$ 328 versus $\phi =$ 440–480 for the cylinders and hexagons). This is again a reflection of the much better streamlined shape of the diamonds (cf. Fig. 2).

To bring the K_v data into agreement, an equivalent cylinder diameter d_{FR} can be defined as the diameter of the cylinders yielding the same flow resistance as the considered hexagons and diamonds. From Eq. (16), d_{FR} is then found as:

$$d_{FR,eq} = \sqrt{\phi_{case\,3} K_{v,case\,3}} \tag{17}$$

The thus obtained values are given in Table 1. Comparing now the entries for case 4 (flow domains with identical d_{FR}) in Table 2 with the entries for the other cases, it can be noted that the case of an identical flow resistance does not correspond to any of the other cases, although one might have expected that the case with identical mean flow-through pore diameter (case 6) would have come close to yielding the same flow resistance. Obviously this is not the case, reflecting the fact that the flow resistance is not only determined by a mean flow-through diameter but is also influenced by the particle shape and the S_p/V_f ratio.

4.2. Species transport and band broadening calculations

For the calculation of the species transport, the most important validity check was on the variation of the peak variance σ_x^2 with the distance x in the flow domain. According to the theory of chromatography, this value is namely expected to vary in a linearly proportional way with x [15]. As can be noted from the example in Fig. 4, this is obviously the case. Fig. 4 also shows that the evolution of the mean peak passage time with the distance is also perfectly linear. Comparing these passage times with the expected passage times calculated on the basis of Eq. (11), the agreement was always closer than 1%, yielding an additional validity check for our calculations.

Fig. 5 shows the obtained plate height versus u_0 curves for all six considered cases. As can be noted, none of the six considered cases corresponds to a condition wherein the three pillar shapes yield the same Van Deemter curve. This implies that none of the presently considered characteristic dimensions can be used as a particle shape-independent basis for the reduction of theoretical plate heights. The pillar system yielding the lowest plate heights also obviously varies from case to case, although for two highly relevant cases, i.e. the case with identical domain size and cross-sectional pillar area (case 3) and the case with identical flow resistance (case 4), the diamond-like pillars yield plate heights which are obviously smaller than the cylinders and the hexagonal pillars.

Given that one of the cases yielding the closest agreement was the identical domain and equivalent particle size case (case 3), all curves were reduced on the basis of d_{eq}, according to:

$$h = \frac{H}{d_{eq}} \quad \text{and} \quad \nu_0 = u_0 \frac{d_{eq}}{D_m} \tag{18}$$

Since all the considered cases and flow domains are obtained by linearly scaling the x- and y-dimensions, leaving the relative dimensions unaltered, it is straightforward to expect that when the six different Van Deemter curves obtained for a given pillar shape are reduced on the basis of their own d_{eq} value (which can be retrieved from the d_{eq} column in Table 2), all reduced curves should coincide. This has been verified and was indeed the case for all three considered pillar shapes. As can be noted from Fig. 6, the diamond-like pillars yield a notably smaller minimal reduced plate height than the cylindrical and hexagonal pillars, and also display a slightly smaller slope in the C-term region of the plot.

To investigate this further, the simulated curves shown in Fig. 6 have been fitted with Knox' well-established reduced plate height expression:

$$h = A\nu_0^{1/3} + \frac{B}{\nu_0} + C\nu_0 \tag{19}$$

Eq. (19) has recently also been confirmed as one of the best fitting correlations during a numerical study of a simulated random packed bed of spheres [8]. The fittings were carried out using the least squares function of Microsoft Excell. The results are shown in Table 3, confirming the slightly smaller C value of the diamond-like pillars. The pillar shape, however, especially seems to have a strong influence on the A term, again in favour of the diamonds ($A \cong 0.06$ for the cylinders and hexagons versus $A \cong 0.03$ for the diamonds). A clear-cut explanation for this finding is currently not available. As expected, the values for B are nearly completely independent of the pillar shape. Further considering the obtained Knox parameters, it is interesting to note that the B and C terms are identical to those traditionally cited for the best possible packed bed [1]. Especially the fact that similar C values are obtained suggests that the currently used characteristic dimension (d_{eq}) provides a good basis of comparison between a 3D packed bed and a 2D pillar array column.

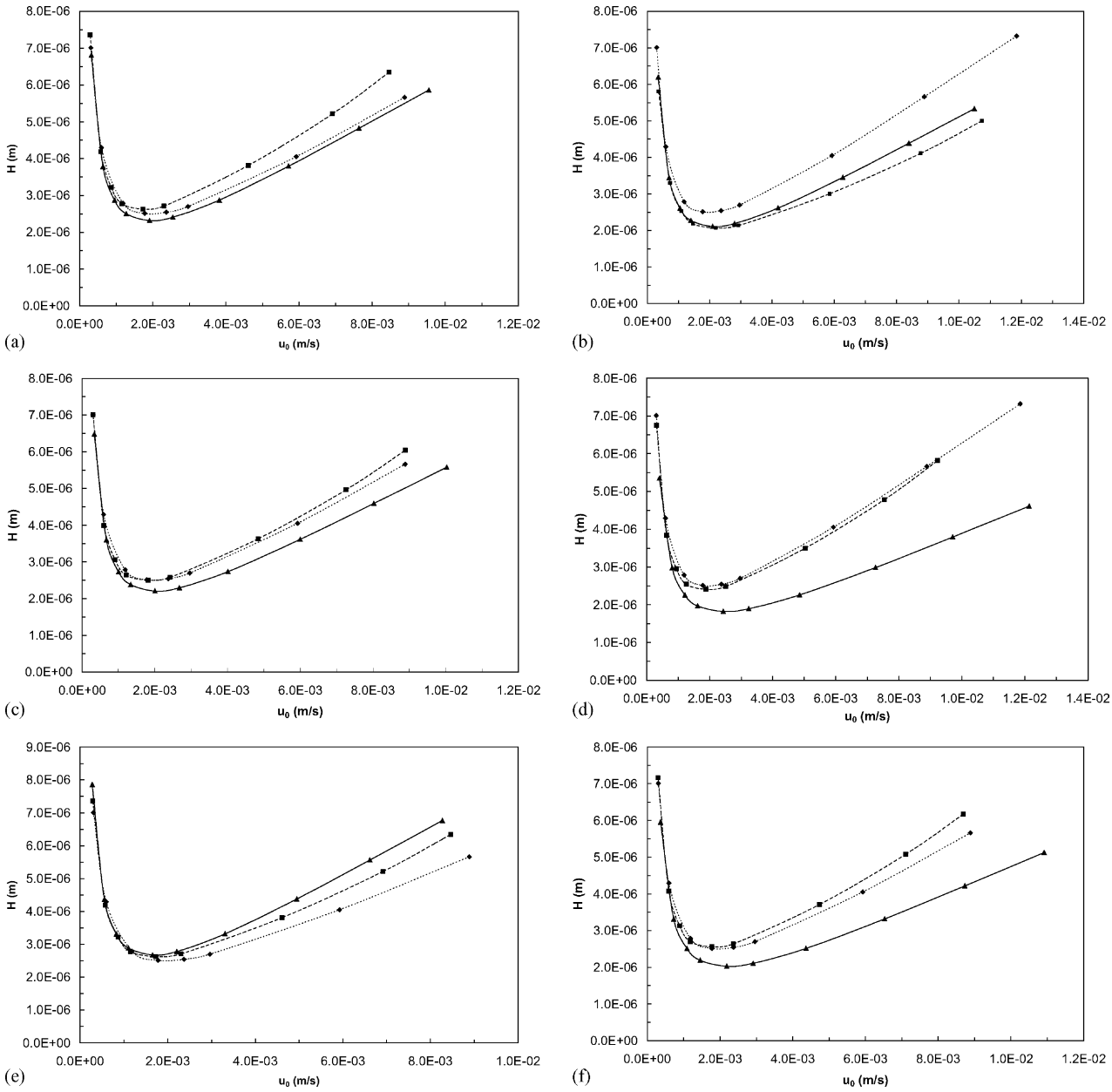

Fig. 5. Comparison of the obtained Van Deemter plots for the three different considered pillar shapes: (a) case 1: identical d_{lat}; (b) case 2: identical $d_{f,min}$; (c) case 3: identical d_{dom}, d_{eq} and A_p; (d) case 4: identical $d_{FR,eq}$; (e) case 5: identical S_p/V_p; (f) case 6: identical $d_{f,mean}$. (■) Cylinders; (◆) hexagons; (▲) diamonds.

The A term values on the other hand are extremely smaller than the $A = 0.5$–1 values typically cited for a packed bed column [17]. Since the A term is known to represent the contribution to band broadening stemming from the irregularities of the packing, the present results can be considered as a strong quantitative argument in favour of the use of highly ordered chromatographic columns. The qualitative argumentations of Knox [1,2] and He et al. [3], lying at the basis of the present study are hence fully substantiated by the present quantitative results.

It should be recalled here that the present findings are independent of any trans-channel coupling effect [15], as the number of flow coupling points is identical for the three different pillar systems considered in Fig. 7.

4.3. Separation impedance

Since it does not require the selection of a characteristic dimension (cf. the first two members of Eq. (3), comparing columns on the basis of the E number is not as difficult as a comparison based on the reduced plate height. Furthermore, since the E number is a direct measure [17] for the analysis time under the condition of a limited pressure drop (which is always the case when pursuing the minimal analysis time),

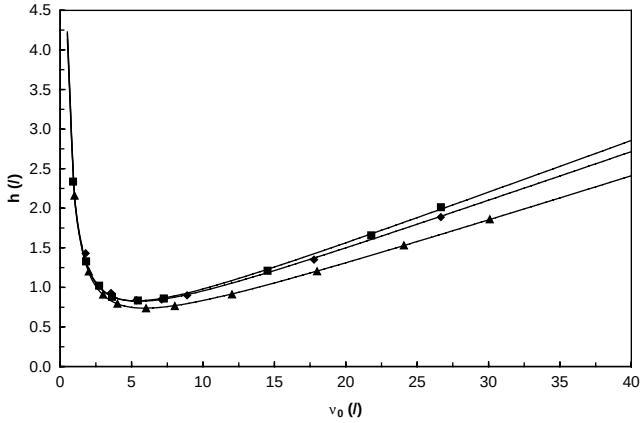

Fig. 6. Reduced Van Deemter plots and fittings with Knox equation (solid lines): (■) cylinders; (◆) hexagons; (▲) diamonds.

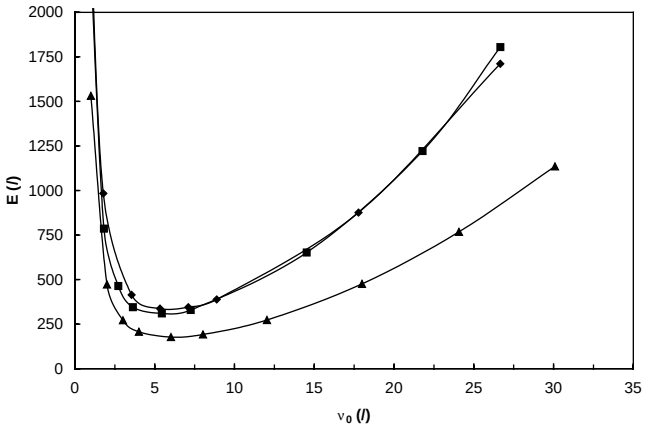

Fig. 7. Separation impedance as a function of the reduced velocity for the three considered pillar shapes: (■) cylinders; (◆) hexagons; (▲) diamonds.

the E number also provides a direct important practical and economic basis of comparison. In this respect, it is highly interesting to note that the presently considered 2D array columns yield E numbers which are more than 10 times smaller the best possible packed bed column for the same bed porosity of $\varepsilon = 0.4$, i.e. without changing the mass loadability and the retention capacity of the system.

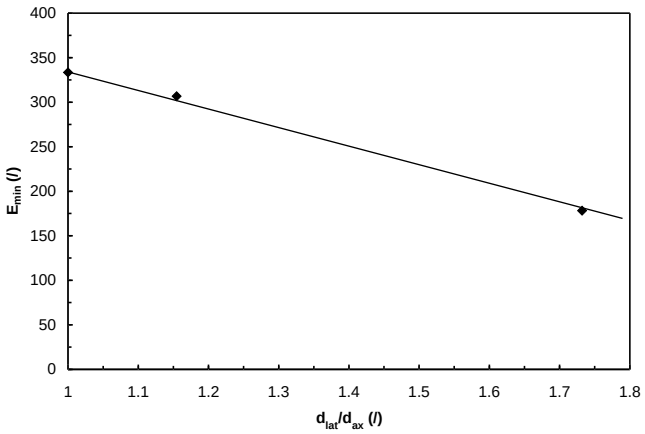

Fig. 8. E_{min} vs. the d_{lat}/d_{ax} ratio of the cylinders ($d_{lat}/d_{ax} = 1$), the hexagons ($d_{lat}/d_{ax} = 1.15$) and the diamonds ($d_{lat}/d_{ax} = 1.73$).

Considering the E_{min} values given in Table 3, we found it instructive to note that there seems to be a clear relation between the degree of axial elongation of the particles (expressed here by the d_{lat}/d_{ax} ratio) and the resulting E number. For the three considered cases, even a linear relationship is obtained (Fig. 8), although it can easily be inferred that this trend cannot be universally valid.

5. Conclusions

The present theoretical study has allowed to gain more insight in the optimal particle shape for 2D etched packed bed columns. Keeping the other geometrical parameters (bed porosity, pillar arrangement) constant, it is found that the "hydrodynamic" shape of the particles has an extremely large impact on the E number. The more axially elongated diamond pillars yield an E_{min} number as small $E_{min} = 180$ (for a retained component with $k'' = 2$), i.e. about 40% smaller than the cylinders and the hexagons ($E_{min} = 300$–330 for $k'' = 2$).

Both the theoretical plate heights ($h_{min} \cong 0.7$–0.8) and separation impedances are significantly smaller than for the best possible packed bed (typically $h_{min} \cong 2$ and $E = 2000$–3000). The fact that 2D etched packed bed columns could yield such small reduced plate height can be attributed to the perfect homogeneity of the flow-through pore network. This is substantiated by the fact that the B and C terms are similar to those in 3D packed bed columns, whereas the A term is about a factor of 10 smaller.

Exploring six different possible characteristic dimension definitions for their potential to bring the Van Deemter plots of the three different particle shapes into agreement, none of them appeared to be valid. This hints at the fact that the definition of such a "universal" characteristic dimension is not straightforward, and that simple assumptions such as the use of an equivalent sphere (or cylinder) diameter based on an identical flow resistance, an approach which is sometimes adopted to compare monolithic and packed bed columns, might not be the ultimate solution.

6. Nomenclature

a	specific external pillar surface ($a = P/A_p$) (m^{-1})
A_{dom}	cross-sectional domain area ($A_{dom} = L_{dom}d_{dom}$) (m^2)
A_f	cross-sectional fluid pore area ($A_f = \varepsilon A_{dom}$) ($m^2$)
A_p	cross-sectional pillar area (m^2)
d_{ax}	maximal pillar dimension in axial direction (parallel to the flow), see Fig. 1 (m)

d_{dom}	domain size, see Fig. 1 (m)
d_{eq}	diameter of cylinder with same cross-sectional area as non-circular pillar, see Eq. (1) (m)
$d_{f,mean}$	mean width of flow-through pores, see Eq. (2) (m)
$d_{f,min}$	minimal width of flow-through pores, see Fig. 1 (m)
$d_{FR,eq}$	equivalent cylinder diameter based on the condition of an identical flow resistance, see Eq. (17) (m)
d_{lat}	maximal pillar dimension in lateral direction (perpendicular to the flow), see Fig. 1 (m)
d_p	cylindrical pillar diameter (m)
d_{ref}	general characteristic pillar dimension (m)
D_m	molecular diffusion coefficient in mobile zone (m^2/s)
D_{sz}	molecular diffusion coefficient in stationary zone (m^2/s)
E	separation impedance, see Eq. (3)
h	reduced theoretical plate height ($h = H/d_{ref}$)
H	height equivalent of a theoretical plate (m)
k_1, k_2	forward and backward rate constant for adsorption reaction in Eq. (6) (s^{-1})
k'	phase retention factor
k''	zone retention factor
k''_0	zone retention factor of unretained species
K	adsorption equilibrium constant ($K = k_1/k_2$)
K_v	column permeability, see Eq. (4) (m^2)
L_{ij}	distance between two different detection planes i and j (m)
P	pillar circumference (m)
ΔP	pressure drop (Pa)
s	side length of hexagons or diamonds (m)
S_p	outer pillar surface (considering a 3D pillar) (m^2)
$t_{R,i}$, $t_{R,j}$	mean passage time at detection planes i and j (s)
u_m	mean velocity of moving fluid = velocity of non-permeating solute (m/s)
u_0	mean velocity of permeating, but non-retained solute (m/s)
V_f	fluid volume (m^3)
V_p	pillar volume (considering a 3D pillar) (m^3)
x	axial position in column (m)

Greek letters

ε	external column porosity
ε_{int}	internal porosity of the porous pillars; $\varepsilon_{int} = 0.5$ in the presented calculations
η	dynamic viscosity (kg/(m s))
ν	reduced fluid velocity, based on u_0 ($=u_0 d_p/D_{mol}$)
ϕ	flow resistance factor

Subscripts

cyl	cylinder
diam	diamond
hex	hexagon
max	maximum
min	minimum

Acknowledgements

The authors greatly acknowledge a research grant (FWO KNO 81/00) of the Fund for Scientific Research—Flanders (Belgium) and support from the IUAP Program on Supra-Molecular Chemistry and Catalysis of the Belgian Federal Government. P.G. is supported through a specialisation grant from the Instituut voor Wetenschap en Technologie (IWT) of the Flanders Region (grant No. SB/11419).

References

[1] J.H. Knox, J. Chromatogr. A 831 (1999) 3.
[2] J.H. Knox, J. Chromatogr. A 960 (2002) 7.
[3] B. He, N. Tait, F.E. Regnier, Anal. Chem. 70 (1998) 3790.
[4] F.E. Regnier, J. High Resolut. Chromatogr. 23 (2000) 19.
[5] B.E. Slentz, N.A. Penner, F. Regnier, J. Sep. Sci. 25 (2002) 1011.
[6] S.V. Ermakov, S.C. Jacobson, J.M. Ramsey, Anal. Chem. 72 (2000) 3512.
[7] J.I. Molho, A.E. Herr, B.P. Mosier, J.G. Santiago, T.W. Kenny, R.A. Brennen, G.B. Gordon, B. Mohammadi, Anal. Chem. 73 (2001) 1350.
[8] M.R. Schure, R.S. Maier, D.M. Kroll, H.T. Davis, Anal. Chem. 74 (2002) 6006.
[9] N. Vervoort, P. Gzil, G.V. Baron, G. Desmet, Anal. Chem. 75 (2003) 843.
[10] Y.X. Wu, C.B. Chin, Chromatographia 56 (2002) 679.
[11] P. Gzil, G.V. Baron, G. Desmet, J. Chromatogr. A 991 (2003) 169.
[12] F.C. Leinweber, D. Lubda, K. Cabrera, U. Tallarek, Anal. Chem. 74 (2002) 2470.
[13] U. Tallarek, F.C. Leinweber, A. Seidel-Morgenstern, Chem. Eng. Technol. 25 (2002) 1177.
[14] F.C. Leinweber, U. Tallarek, J. Chromatogr. A 1006 (2003) 207.
[15] J.C. Giddings, Dynamics of Chromatography. Part I, Marcel Dekker, New York, 1965.
[16] M. Kaviany, Principles of Heat Transfer in Porous Media, 1st ed., Springer, New York, 1995.
[17] J.H. Knox, J. Chromatogr. Sci. 18 (1980) 453.